Structure and Dynamics of Supported Intermembrane Junctions

Yoshihisa Kaizuka and Jay T. Groves
Department of Chemistry, University of California, Berkeley, California

ABSTRACT Supported intermembrane junctions, formed by rupture of giant unilamellar vesicles onto conventional supported lipid membranes, have recently emerged as model systems for the study of biochemical processes at membrane interfaces. Using intermembrane fluorescence resonance energy transfer and optical standing wave fluorescence interferometry, we characterize the nanometer-scale topography of supported intermembrane junctions and find two distinct association states. In one state, the two membranes adhere in close apposition, with intermembrane separations of a few nanometers. In the second state, large intermembrane spacings of ~50 nm are maintained by a balance between Helfrich (entropic) repulsion and occasional sites of tight adhesion that pin the two membranes together. Reversible transitions between these two states can be triggered with temperature changes. We further examine the physical properties of membranes in each state using a membrane mixture near its miscibility phase transition temperature. Thermodynamic characteristics of the phase transition and diffusive mobility of individual lipids are comparable. However, collective Brownian motion of phase-separated domains and compositional fluctuations are substantially modulated by intermembrane spacing. The scaling properties of diffusion coefficient with particle size are determined from detailed analysis of domain motion in the different junction types. The results provide experimental verification of a theoretical model for two-dimensional mobility in membranes, which includes frictional coupling across an interstitial water layer.

INTRODUCTION

Highly organized and communicative junctions between cells are a definitive feature of multicellular organisms. Geometrical confinement on molecular length scales, which is inherent to intercellular junctions, has profound consequences on the biochemical reactions that take place in these spaces. For example, the reaction between populations of receptors and ligands at the T-cell immunological synapse gives rise to self-assembling patterns of proteins, which play a functional role in the ensuing signal transduction (Davis, 2002; Grakoui et al., 1999; Krummel and Davis, 2002; Lee et al., 2002a; McCann et al., 2002; Monks et al., 1998; Stoll et al., 2002; vanderMerwe, 2002; vanderMerwe and Davis, 2002). This reaction-induced pattern formation results from intimate cooperativity between protein binding and mechanical constraints from the membrane and cytoskeleton, which leads to size-based lateral sorting of proteins within their respective fluid membranes (Lee et al., 2003, 2002b; McCann et al., 2003; Qi et al., 2001). The rich complexity of chemistry that emerges at intermembrane junctions can often be traced to interplay among a small number of physical and chemical effects, rendering these systems tractable to quantitative mechanistic interpretation.

There is significant interest in the development of model systems to facilitate precise analysis of reaction processes at intermembrane junctions. Many strategies have employed lipid membranes supported on solid substrates (Groves and Boxer, 2002; Groves and Dustin, 2003; Sackmann, 1996; Sackmann and Tanaka, 2000). In this configuration, an ~1-nm layer of water between the membrane and the substrate preserves free lateral diffusivity of individual molecules. Supported membranes have been employed to reconstitute elaborate cell surface interactions with remarkable success. A notable example is provided by the formation of an immunological synapse between a living T cell and a supported membrane containing the relevant cognate receptors (Grakoui et al., 1999; Hailman et al., 2002). Model intermembrane junctions, in which both membranes are reconstituted, have been created with supported membranes by several methods. Junctions can be formed by allowing intact giant unilamellar vesicles (GUVs) to interact with supported membranes (Albersdörfer et al., 1997; Bruinsma et al., 2000; Kloboucek et al., 1999; Sackmann and Bruinsma, 2002). Alternatively, two membranes can be deposited onto a solid substrate by successive transfer of four monolayers from an air-water interface (Charitat et al., 1999; Fragneto et al., 2001). In the following, we study the properties of intermembrane junctions, which are formed by rupture of GUVs onto supported membranes (Wong and Groves, 2001). This technique produces planar junctions, typically 10–100 μm in lateral extent, that are well suited to fluorescence imaging techniques.

Structural resolution of the intermembrane junctions is accomplished using a combination of fluorescence techniques, which provide real-time imaging of membrane topographical patterns. Intermembrane fluorescence resonance energy transfer (FRET) occurs between membranes, which have been doped with complementary fluorescent probes, when the intermembrane spacing is comparable to the Förster distance for the probe pair (~5 nm). Quantitative analysis of FRET efficiency provides measurement of intermembrane spacing with subnanometer precision in closely

Submitted June 30, 2003, and accepted for publication October 3, 2003.

Address reprint requests to Jay T. Groves, Dept. of Chemistry, University of California, Berkeley, CA 94720. Tel.: 510-643-0186; Fax: 510-642-8821; E-mail: JTGroves@LBL.GOV.

0006-3495/04/02/905/08 $2.00

spaced membrane junctions (Wong and Groves, 2002). Measurements of intermembrane spacings beyond the range of FRET is achieved using fluorescence interference contrast microscopy (FLIC) (Lambacher and Fromherz, 1996, 2002; Wong and Groves, 2001). This technique exploits the spatial intensity variation within an optical standing wave to modulate the fluorescence intensity of probes as a function of their position along the optical axis, which is perpendicular to the interface in this configuration. FLIC achieves nanometer resolution and can resolve topographical structures extending hundreds of nanometers from the primary plane. In combination, these two imaging techniques vividly reveal the dynamic topographical and lateral structure of intermembrane junctions.

Two distinctively different states of intermembrane junction are observed in the experiments described below (Fig. 1). Uniform intermembrane separation distances of a few nanometers characterize the first state, here referred to as *Type 1*. In the second state (*Type 2*), intermembrane spacings are ~50 nm and FLIC imaging reveals large-scale thermal undulations of the membrane. Correspondence between the structures described here with those observed by reflection interference contrast microscopy (Albersdörfer et al., 1997; Kloboucek et al., 1999) and neutron reflectivity (Charitat et al., 1999; Fragneto et al., 2001; Mecke et al., 2003) in other systems are discussed.

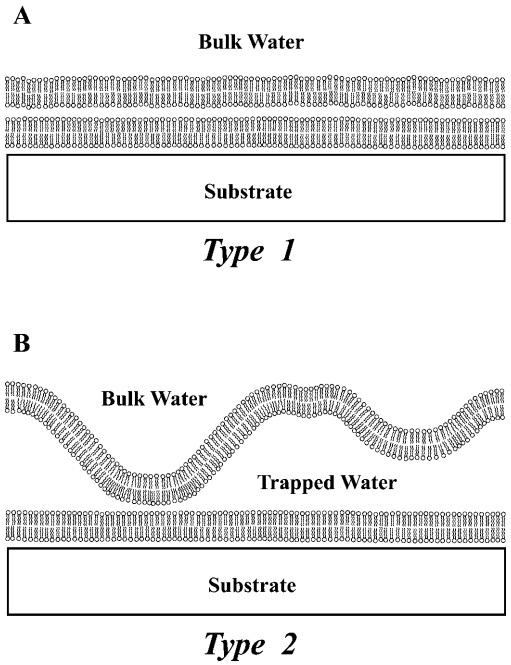

FIGURE 1 (*A*) Schematic illustration of a Type 1 junction; intermembrane separation distances are typically 2–3 nm. (*B*) Schematic of a Type 2 junction. Average intermembrane separation distances are ~50 nm and marked thermal undulation of the membrane occurs. Occasional adhesion sites pin the upper membrane in place.

The physical properties of membranes in the different types of junction are compared using a phase-separating mixture of phosphatidylcholine (PC), cholesterol, and sphingolipid. Below the miscibility transition temperature, the mixture separates into coexisting liquid phases, which can be resolved by fluorescence microscopy. Collective motion of phase-separated domains in the two junction types differ substantially. Comprehensive measurements of domain diffusion are compared with calculations using a theoretical model for the translational drag experienced by a disk moving in a liquid membrane near a solid interface (Evans and Sackmann, 1988; Merkel et al., 1989). The model yields relatively accurate predictions of the differential size scaling of diffusion coefficient in terms of the thickness of the interstitial water layer. Experimental verification of this model over multiple length scales provides a quantitative framework to consider coupling of membrane properties in a variety of systems, including intercellular junctions.

MATERIALS AND METHODS

Dimyristoylphosphatidylcholine (DMPC), dioleoylphosphatidylcholine (DOPC), dioleoylphosphatidylserine (DOPS), dioleoyltrimethylammonium-propane (DOTAP), cholesterol, egg sphingomyelin, and 1-palmitoyl-2-[12-[(7-nitro-2-1,3-benzoxadiazol-4-yl)amino]dodecanoyl]-*sn*-glycero-3-phosphocholine (NBDPC) were obtained from Avanti Polar Lipids (Alabaster, AL). Texas Red dipalmitoylphosphatidylethanolamine (Texas Red DPPE) was obtained from Molecular Probes (Eugene, OR). Monosialoganglioside (GM_1) was obtained from Matreya (Pleasant Gap, PA). All lipids were dissolved in chloroform except sphingomyelin and GM_1, which were dissolved in 2:1 chloroform and methanol.

Solid supported lipid bilayer membranes were formed by fusion of small unilamellar vesicles (SUVs) onto the substrates. Glass coverslips were used for fluorescence microscopy and cleaved silicon wafer chips, with either 2-nm (native) or 100-nm silicon oxide layers, were used for FLIC. SUVs were prepared by sonication. A dried lipid film of the mixture containing 88 mol % DMPC, 10 mol % DOTAP, and 2 mol % NBDPC was formed on a round-bottom flask. The lipid film was hydrated in deionized water at ~1 mg/ml (lipid concentration) and then probe-sonicated for ~90 s, until the solution became clear. The resulting dispersion was purified by ultracentrifuge for 2.5 h at 166,000 *g*; the supernatant contained SUVs. A 1:1 mixture of SUV solution and phosphate-buffered saline (PBS) was spread over the surface of glass coverslips or silicon wafer chips, which had been etched in piranha solution (3:1 freshly mixed sulfuric acid and hydrogen peroxide) shortly before use. Supported membranes formed rapidly; excess SUVs were rinsed from the sample.

GUVs were prepared in similar fashion to Akashi et al. (1996), with some simplifications. A 1.5:1:1 mixture of DOPC, cholesterol, and egg SM doped with 1 mol % GM_1, 5 mol % DOPS, and 0.6 mol % Texas Red DPPE was dried in a small glass test tube. DOPS is included to facilitate membrane junction formation via electrostatic adhesion. GM_1 facilitates Type 2 junction formation, presumably by reducing some of the intermembrane attractions. The dried lipid film was then suspended at ~0.5 mg/mL (lipid concentration) in 0.5 M sucrose solution, prewarmed to 42°C. The samples were incubated at 42°C for 2 h, and gradually cooled to room temperature. A floating cloud of lipids containing concentrated GUVs, 10–20 μm in diameter, was observed in successful preparations. Multilamellar vesicles are also formed during this preparation. However, they are readily distinguishable from GUVs and only GUVs were used for observation. GUVs were deposited onto supported membranes in deionized water or onto

glass coverslips in twice-diluted PBS (80-mM ionic strength). Rupture of GUVs upon contact with supported membranes formed intermembrane junctions.

Supported intermembrane junctions were viewed with a Nikon TE300 inverted fluorescence microscope (Nikon, Tokyo, Japan) equipped with a mercury arc lamp. Images were recorded with a cooled charge-coupled device camera (Hamamatsu C4742-98 ORCAII, Hamamatsu, Japan) through a Nikon 100× oil-immersion objective (adjustable aperture set to $NA = 1.0$) or 60× extra-long working distance objective ($NA = 0.7$). The sample temperature was measured and controlled by a BioScope Fluid Sample Heater (Veeco, Santa Barbara, CA). Image data was analyzed with Simple PCI (Compix, Cranberry Township, PA) and home-written programs.

FRET efficiency was analyzed to determine intermembrane separation distances as described previously (Wong and Groves, 2002). Briefly, the rate, k_T, of nonradiative energy transfer from a donor to a population of acceptors, which are distributed in an offset plane, is given by

$$k_T = \frac{\sigma\pi R_0^6}{2\tau_D z^4}, \tag{1}$$

where σ is the concentration of acceptor molecules, R_0 is the Förster distance (5 nm for the Texas Red-NBD pair; Lakowicz, 1999), τ_D is the fluorescence lifetime of the donor in the absence of acceptors, and z is the separation distance between the donor and the plane of acceptors. Two leaflets of the bilayer membrane result in two planes of acceptors, separated from each other by ~4 nm. The tail-labeled NBDPC donors, which preferentially localize in the glycerol/upper chain region of the membrane (Huster et al., 2001), are taken to occupy a single plane. The total FRET efficiency, E, is obtained by summing up the different transfer pathways, denoted with primes:

$$E = \frac{k_T' + k_T''}{k_T' + k_T'' + 1/\tau_D}. \tag{2}$$

Analysis of FRET efficiency using Eqs. 1 and 2 directly provides the separation distance between probe molecule planes. To estimate the intermembrane separation, we subtract 2 nm to account for embedding of the probe within the membrane. FRET analysis in phase-separated membranes requires determination of the local acceptor probe concentration in each phase. For the membrane mixture studied here, we determined that the PC-rich phase constitutes ~40% of the membrane area at room temperature; the probe concentrations in the PC-rich and cholesterol-rich phases were ~1% and 0.3%, respectively.

FLIC intensity images were deconvolved into three-dimensional topography data using the simplified relation for fluorescence intensity, F,

$$F \propto \left(2(1-r_f)^2 + 8r_f \sin^2\left(\frac{\phi_{ex}}{2}\right)\right) \times \left(2(1-r_f)^2 + 8r_f \sin^2\left(\frac{\phi_{em}}{2}\right)\right), \tag{3}$$

which is derived from basic optical principles (Born and Wolf, 1999). The arguments, ϕ_{ex} and ϕ_{em}, are given by $(4\pi/\lambda_{ex})(n_w z + n_0 z_0)$ and $(4\pi/\lambda_{em})(n_w z + n_0 z_0)$, respectively. Indices of refraction for water (1.33) and silicon oxide (1.46) are represented by n_w and n_0, z is the height above the oxide surface, and z_0 is the oxide thickness. The excitation and emission wavelengths, λ_{ex} and λ_{em}, are 560 and 645 nm, when using the Texas Red fluorophore. The reflection coefficient of the silicon-silicon oxide interface (0.46 at 645 nm) is represented by r_f. This approximation has a maximum error of ~2 nm over the distance range of these experiments, compared to more involved calculations that include the angular spread of incident and collected light as well as spectral bandwidth (Lambacher and Fromherz, 1996, 2002).

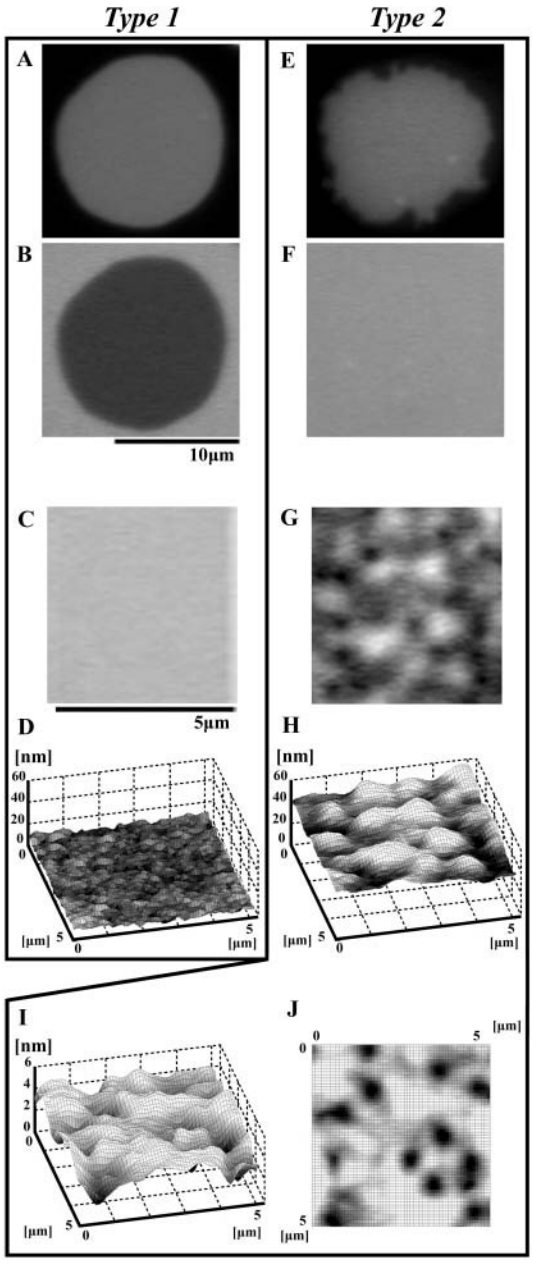

FIGURE 2 Texas Red fluorescence from the upper membrane (*A*) and NBD fluorescence from the lower membrane (*B*) in a Type 1 junction. The measured FRET efficiency of 0.41 with an acceptor concentration of 1% corresponds to a probe separation distance of 4.4 nm and an estimated intermembrane water layer of ~2.4 nm. FLIC image of the upper membrane (*C*) and corresponding topography plot (*D*) from a Type 1 junction. A Type 2 junction viewed by Texas Red fluorescence from the upper membrane (*E*), NBD fluorescence from the lower membrane (*F*), and FLIC of upper membrane (*G*) with corresponding topography plot (*H*). The mean intermembrane separation distance determined from these FLIC images is 46 nm. *I* and *J* illustrate plots of RMS fluctuation amplitude from the region depicted in *G*. The dark regions in *J* map areas of reduced fluctuation, which correspond to pinning sites.

RESULTS AND DISCUSSION

Junction types

Fluorescence images of two types of intermembrane junction are depicted in Fig. 2. Fluorescence from the upper membrane in Fig. 2 *A* corresponds to a footprint of reduced fluorescence in the lower membrane (Fig. 2 *B*). This results from FRET between energy donors (NBDPC) in the lower membrane and acceptors (Texas Red DPPE) in the upper membrane. Efficient FRET is indicative of intermembrane separation distances of a few nanometers (Wong and Groves, 2002), and is a definitive feature of Type 1 junctions. The FRET efficiency of the footprint in Fig. 2 *B* is 0.41, uniformly, with the acceptor concentration of 1% in the upper membrane. This corresponds to a constant separation distance between the probe planes of 4.4 nm and an estimation of ~2.4 nm for the water layer between the two membranes in this Type 1 junction (see Materials and Methods for details). FLIC images of upper membranes in Type 1 junctions (Fig. 2, *C* and *D*) reveal flat surfaces as well. Although direct fluorescence images of upper membranes in Type 2 junctions (Fig. 2 *E*) appear equivalent to those of Type 1, intermembrane FRET and FLIC reveal a very different situation.

A definitive feature of Type 2 junctions is the absence of any intermembrane FRET (Fig. 2 *F*), which indicates that intermembrane separation distances are in excess of 10 nm. Fig. 2 *G* is a representative FLIC image of the (upper) membrane surface of a Type 2 junction, capturing the actual membrane topography at a moment (20 ms) in time. The corresponding three-dimensional reconstruction of the surface is shown in Fig. 2 *H* (see Materials and Methods for details). Membrane topographical undulations (~4 nm RMS amplitude, ~340 nm lateral spatial correlation length) fluctuate with a characteristic relaxation time of ~1 s. The mean separation distance between upper and lower membranes in Type 2 junctions is typically ~50 nm. The specific Type 2 junction pictured in Fig. 2 has a 46-nm mean separation distance, as determined by FLIC imaging. Fig. 2, *I* and *J*, are plots of the mean fluctuation amplitude over the region shown in Fig. 2, *G* and *H*. These data, which are generated by averaging data from FLIC images of the membrane taken at different times, reveal occasional fixed adhesion sites (reduced fluctuation amplitude) that serve to pin the two membranes together. No corresponding intermembrane FRET is visible (Fig. 2 *F*), establishing that the lateral extent of each adhesion site is well below the optical detection limit of ~100 nm.

Reversible transitions between the two junction types could be triggered by temperature changes. Higher temperatures favor the Type 2 junctions, which is consistent with a role for Helfrich repulsion (Lipowsky and Sackmann, 1995) in the stabilization of this structure. These transitions are restricted by the requirement of water flow in the intermembrane space. That is, the uniformly distributed water layer in Type 2 junctions becomes corralled into taut blisters (Nardi et al., 1998; Wong and Groves, 2001) during the transition to a Type 1 junction. Similarly, flow of water under the membrane limits the transition to Type 2. An analysis of fluid dynamics within the intermembrane space and its effect on structures of membrane junctions is described elsewhere (Parthasarathy et al., 2004).

The junction types observed here qualitatively correspond to the two adhesion states that Sackmann and co-workers report at contacts between flaccid GUVs and supported membranes (Albersdörfer et al., 1997; Kloboucek et al., 1999). It has been postulated that the intermembrane potential energy can have a double minimum, which gives rise to two adhesion states (Bruinsma et al., 2000). However, it is not necessary that a true second minimum in the interaction potential is responsible for the stable Type 2 junctions we observe. Intermembrane spacings of ~50 nm are expected to be well outside the range of any attractive interaction; membranes are held in the Type 2 configuration by occasional pinning sites. The structures Graner and co-workers describe in membrane junctions formed by Langmuir transfer fall within the Type 1 category (Charitat et al., 1999; Fragneto et al., 2001; Mecke et al., 2003).

Lateral mobility

To characterize the membrane physical properties within the different junction types, we examine a phase-separating mixture of PC, cholesterol, and sphingolipid as a paradigmatic test case. GUVs prepared from a 1.5:1:1 mixture of these components separate into coexisting liquid phases at room temperature and remix to homogeneity above the miscibility transition temperature of ~33°C (Dietrich et al., 2001; Veatch and Keller, 2002). Below the transition temperature, two phases can be readily distinguished by

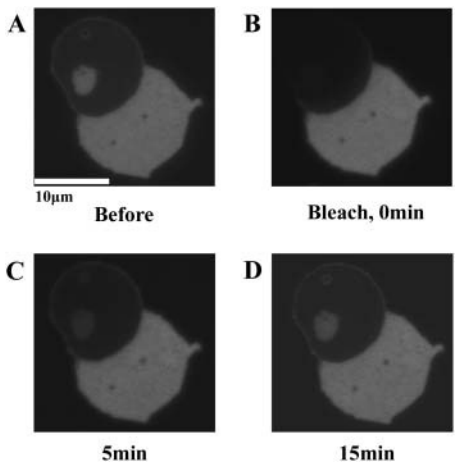

FIGURE 3 FRAP experiment on a phase-separated patch of membrane formed by rupture of a GUV directly onto a glass coverslip. (*A*) Original membrane patch before bleaching. *B*, *C*, and *D* depict images of the same patch immediately, 5 min, and 15 min after the bleach period.

preferential partitioning of the fluorescent probe lipid (Texas Red DPPE) into the more disordered, PC-rich phase. In the following, phase-separated GUVs are used to form Type 1 and Type 2 junctions, as well as to deposit phase-separated bilayer structures directly onto the substrate.

Fig. 3 depicts results from a fluorescence recovery after photobleaching experiment (FRAP), performed on a phase-separated patch of supported membrane. This patch was formed by allowing a phase-separated GUV to burst directly onto the substrate. The precursor GUV consisted of a large domain of the PC-rich phase (*bright*) and a large domain of the cholesterol-rich phase (*dark*). A smaller island of the PC-rich phase is trapped within the cholesterol-rich domain. This configuration allows characterization of lipid mobility in both the PC-rich and the cholesterol-rich phases. An image of the isolated membrane patch before any photobleaching is illustrated in Fig. 3 *A*. The photobleaching illumination was focused onto the cholesterol-rich domain, bleaching probes in the enclosed PC-rich island as well as probes within the cholesterol-rich phase. The probe concentration in this phase was measured to be roughly 1/3–1/5 of that in the PC-rich phase, based on fluorescence intensity. The bleached membrane is shown in Fig. 3 *B*. The state of the membrane at 5 and 15 min after bleaching is illustrated in Fig. 3, *C* and *D*, respectively. Recovery of fluorescence in the PC-rich island reveals diffusive mixing between probes in this region and those in the larger PC-rich domain, despite the fact that these two regions are not connected. Probes diffuse through the cholesterol-rich phase. Diffusion coefficients within cholesterol-rich phases, similar to the one studied here, have been measured by fluorescence correlation spectroscopy to be $\sim$0.3 $\mu m^2/s$; $\sim$10-fold higher mobilities were measured in PC-rich phases (Kahya et al., 2003). Despite free diffusion throughout both phases, the overall shape and position of the domains remains static.

Observation of phase-separated domains in Type 1 junctions reveals diffusive equilibration without significant collective motions, comparable to observations in supported membranes described above. Fig. 4, *A* and *B*, depict lower and upper membranes of a Type 1 junction, respectively. FRET efficiency measurements from this junction correspond to a probe separation distance of 4.8 nm, from which we estimate the intermembrane water layer to be $\sim$2.8 nm. The upper membrane was deposited from a phase-separated GUV (same composition as above), and dark cholesterol-rich domains are clearly visible. Fig. 4, *B–F*, are a time sequence of images of the upper membrane that reveal diffusive equilibration of the phase-separated domains. Smaller domains grow smaller and evaporate altogether, whereas larger domains grow still larger in an Ostwald ripening process (Domb and Lebwitz, 1988).

Phase-separated domains in the upper membranes of Type 2 junctions exhibit rapid Brownian motion and are also observed to collide and coalesce. Fig. 5 *A* is a fluorescence

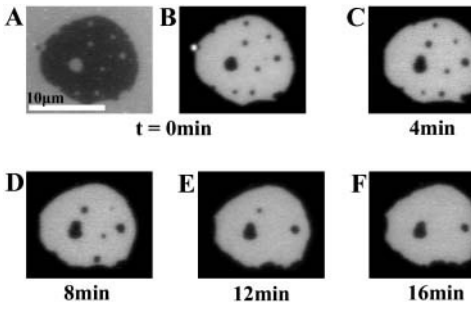

FIGURE 4 Diffusive equilibration of phase-separated domains in a Type 1 junction. A FRET footprint in the NBD fluorescence from the lower membrane (*A*) corresponds to the phase-separated domains seen in Texas Red fluorescence of the upper membrane (*B*). The FRET efficiency is 0.33, the effective Texas Red concentration in the PC-rich phase is $\sim$1%, the separation distance between probe molecules in the two membranes is calculated to be 4.8 nm, and the interstitial water layer is estimated to be $\sim$2.8 nm. *C–F* are images of the upper membrane at subsequent times, as labeled.

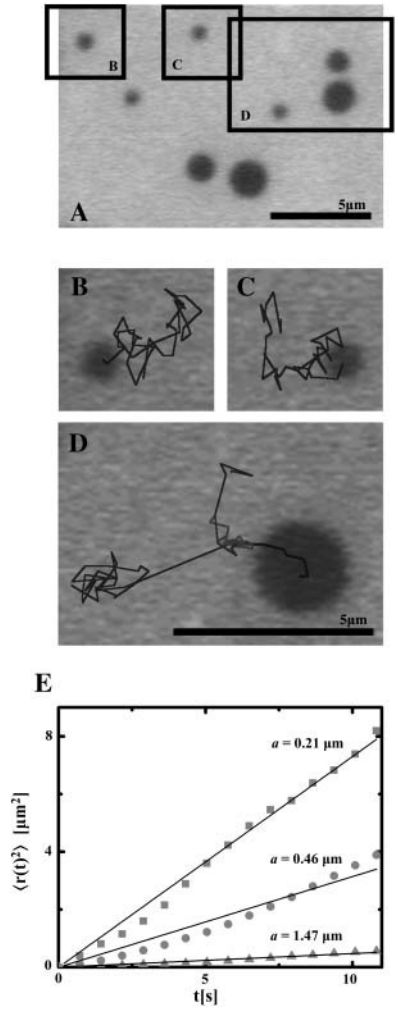

FIGURE 5 Brownian motion of phase-separated domains in a Type 2 junction. (*A*) Fluorescence image of a collection of cholesterol-rich domains (*dark*) within the PC-rich phase. *B–D* depict Brownian trajectories (0.7-s intervals) for domains from *A* (as labeled). Note that three domains collide and coalesce into one in *D*. (*E*) Plots of $\langle r(t)^2 \rangle$ for three representative domains.

image of a region of upper membrane in a Type 2 junction, which was prepared from a phase-separated GUV. Multiple round cholesterol-rich domains can be observed to undergo two-dimensional Brownian motion within the PC-rich phase. Brownian trajectories measured for several of the domains in Fig. 5 *A* are depicted in Fig. 5, *B–D*, as labeled. Note that three domains collide to form one, still circular, domain in the sequence plotted in Fig. 5 *D*. We quantify domain mobility by measuring the mean-square displacement, $\langle r(t)^2 \rangle$ (where t represents the step time interval), of each domain throughout its Brownian trajectory. Representative plots of $\langle r(t)^2 \rangle$ for several domains of differing size are depicted in Fig. 5 *E*. Detailed analysis of 79 domains, constituting all domains in the field of view from a representative Type 2 junction, revealed 36 domains for which $\langle r(t)^2 \rangle$ scaled approximately linearly with t, as shown in Fig. 5 *E*. The remaining 43 domains exhibited trapped diffusion, ricocheting within corrals of pinning centers, which was manifest as nonlinear and bounded $\langle r(t)^2 \rangle$. Data from freely diffusing domains are used in the following analysis.

The diffusion of a disk within a two-dimensional fluid, such as a lipid membrane, is described by

$$\langle r(t)^2 \rangle = 4Dt = 4\frac{k_B T}{\lambda}t, \tag{4}$$

where D is the diffusion coefficient, k_B is the Boltzmann constant, T is the temperature, and λ is the drag coefficient. Equation 4 is a statement of the Einstein relation ($\lambda = k_B T/D$), which is valid as long as the drag scales linearly with velocity (λ is independent of velocity). Calculation of drag for membranes is complicated by the fact that there are no solutions to the slow viscous flow equations for steady translational motion in two dimensions (Stokes paradox), in contrast to three-dimensional systems. This implies that the drag on a particle in two-dimensional hydrodynamics is intrinsically nonlinear with velocity, which would invalidate the Einstein relation (contrary to observation). The paradox is broken in real systems by coupling of membrane flow to flow in the surrounding, three-dimensional fluid; theory (Hughes et al., 1981; Saffman, 1976; Saffman and Delbrück, 1975) and experiment (Klingler and McConnell, 1993a,b) are in good agreement for membranes bounded by infinite fluid phases.

An approximate drag coefficient for a two-dimensional fluid with frictional coupling to a nearby solid substrate has been described (Evans and Sackmann, 1988; Merkel et al., 1989),

$$\lambda = 4\pi\eta_m z_m \left(\frac{\varepsilon^2}{2} + \frac{\varepsilon K_1(\varepsilon)}{K_0(\varepsilon)}\right), \tag{5}$$

where η_m is the membrane viscosity (10^{-1} Ns/m^2; Evans and Skalak, 1980), and z_m is the membrane thickness (4 nm). K_0 and K_1 are modified Bessel functions of the second kind. The nondimensional radius, ε, is given by

$$\varepsilon = a\sqrt{\frac{b_s}{\eta_m z_m}}, \tag{6}$$

where a is the disk radius and b_s is a frictional coefficient. We approximate b_s as $\alpha\eta_w/z_w$, where η_w is the viscosity of water (10^{-3} Ns/m^2 at 20°C) and z_w is the thickness of the intermembrane water layer. This approximation is expected to be valid for $z_w \ll \eta_m z_m/\eta_w \approx 400$ nm, the characteristic depth of the flow-field region adjacent to the membrane. The empirical proportionality constant, α, is set to 2 for the best agreement with our experimental results.

Calculations of D as a function of disk radius from Eqs. 4–6 are plotted in Fig. 6 along with measured values of D for domains in representative Type 1 and Type 2 junctions. Calculations of D for membranes bounded by infinite water phases (purely hydrodynamic drag), following the methods of Hughes et al. (1981), are also plotted for comparison. All three calculations predict essentially equivalent molecular diffusion (within a factor of 2), but exhibit different scaling behavior with particle size. The frictional coupling model accurately predicts the diffusion coefficient scaling we observe in the Type 2 junctions ($z_w \approx 50$ nm), and further predicts greatly reduced mobility of large phase-separated domains in the Type 1 junctions ($z_w \approx 2.8$ nm). The calculated diffusion coefficients for Type 1 junctions trace an upper bound on the measured values. We attribute the large variability in measured values in Type 1 junctions to the likely existence of surface defects, through which the domains must flow in order to move.

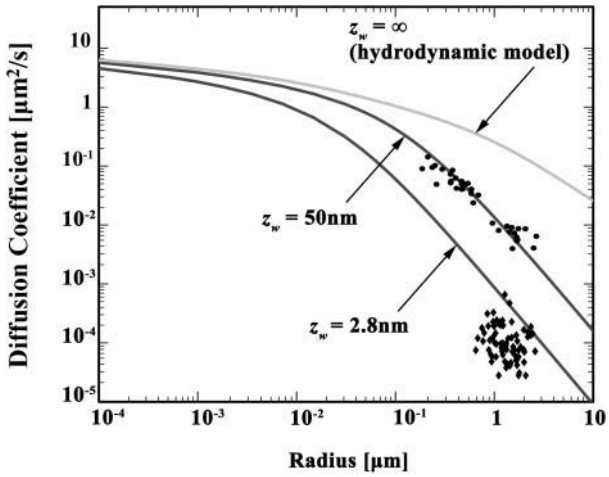

FIGURE 6 Calculations of diffusion coefficient versus particle size, from the diffusion models described in the text, are plotted along with measured values of domain diffusion in Type 1 (♦) and Type 2 (●) junctions. 75 of 117 domains in the field of view of the representative Type 1 junction and 36 of 79 domains in the representative Type 2 junction exhibited approximately linear scaling of $\langle r(t)^2 \rangle$ with t and are plotted here. As a consequence of ongoing Ostwald's ripening, accurate diffusion measurements of the smallest domains could not be made in Type 1 junctions.

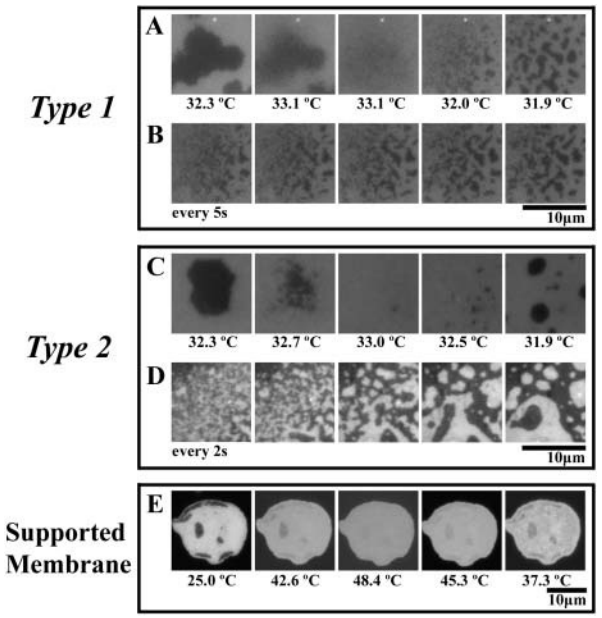

FIGURE 7 Miscibility phase transitions, triggered by temperature changes, in a Type 1 (*A*, *B*), a Type 2 (*C*, *D*), and a conventionally supported membrane (*E*). *B* and *D* are time sequences of demixing transitions taken at 5-s and 2-s intervals, respectively. The irregularly shaped domain in the initial image of *A* (Type 1) was trapped in that configuration during rupture of the GUV. The irregularly shaped domain in the initial image of *C* (Type 2) is undergoing rapid shape fluctuations. Large collective motions contribute to the mixing and demixing transitions in Type 2 junctions (*C*, *D*) whereas the transitions are primarily diffusive in Type 1 junctions (*A*, *B*).

Phase transitions

Temperature-induced mixing and demixing phase transitions exhibit similar behavior in the two junction types. An initially phase-separated state is created by rupturing a phase-separated GUV, below the miscibility transition temperature. Fig. 7 illustrates a series of images from three representative experiments depicting the miscibility phase transition in the upper membranes of Type 1 (Fig. 7, *A* and *B*) and Type 2 (Fig. 7, *C* and *D*) junctions as well as a supported membrane (Fig. 7 *E*). The transition temperatures for both Type 1 and Type 2 junctions are essentially identical (~33°C). Type 1 junctions above the transition temperature are particularly vulnerable to intermembrane mixing, which can alter the composition and change the transition temperature. Consistently accurate transition temperature measurements were made by minimizing the amount of time the sample was held in the homogeneous state. In the supported membrane, it proved difficult to achieve a complete miscibility transition. Note that the domains return in the same positions as in the initial state. The persistence of substrate-stabilized structures can complicate transition temperature measurements. The apparent transition in the supported membrane pictured in Fig. 7 *E* is ~45°C, compared to ~33°C for the same composition in upper membranes from both Type 1 and Type 2 junctions. Fig. 7, *B* and *D*, are time sequences of images illustrating the process of phase separation in the two junction types. Images were taken at 5-s intervals for the Type 1 junction and 2-s intervals for the Type 2 junction. Collective motions in Type 2 junctions enable rapid coarsening of compositional fluctuations, a characteristic of spinodal decomposition (Papon et al., 2002), during the demixing transition. This process also occurs in Type 1 junctions, but is more difficult to observe. Greater freedom of movement in Type 2 junctions also facilitates the formation of larger phase-separated domains.

CONCLUSIONS

The structure and dynamical properties of two types of supported intermembrane junction have been analyzed. Type 1 junctions, characterized by apposition of the two membranes within a few nanometers, are distinguishable by efficient intermembrane FRET and lack of resolvable topography in the upper membrane. Type 2 junctions are more widely spaced (~50 nm), do not show intermembrane FRET, and exhibit marked thermal undulations, which can be resolved by FLIC microscopy. A differential scaling of lateral mobility with size was observed in the two junction types. Whereas molecular diffusion is similar in both junction types, collective Brownian motion of phase-separated domains is 1–2 orders-of-magnitude faster in the upper membranes of Type 2 junctions. A quantitative model for diffusion in membranes associated with solid substrates (Evans and Sackmann, 1988) can describe this differential scaling of mobility in terms of the thickness of the interstitial water layer. Miscibility phase transitions exhibit generally similar behavior in the upper membranes of both Type 1 and Type 2 junctions. In contrast, the silica substrate was observed to interfere with transitions in conventionally supported membranes. The supported membrane junctions described here provide a useful system for study of intermembrane reaction processes. Additionally, the upper membranes in these junctions are relatively more free of substrate influences than supported membranes, and may thus be of use for general studies of membrane physical properties.

We thank Dr. Raghuveer Parthasarathy for helpful discussions and Amy P. Wong for her involvement in the experimental genesis of this work.

This work was supported in part by National Institutes of Health grant 1-R01-GM64900-01 and the Burroughs Wellcome Career Award in the Biomedical Sciences.

REFERENCES

Akashi, K., H. Miyata, H. Itoh, and K. Kinosita. 1996. Preparation of giant liposomes in physiological conditions and their characterization under an optical microscope. *Biophys. J.* 71:3242–3250.

Albersdörfer, A., T. Feder, and E. Sackmann. 1997. Adhesion-induced domain formation by interplay of long-range repulsion and short-range attraction force: a model membrane study. *Biophys. J.* 73:245–257.

Born, M., and E. Wolf. 1999. Principles of Optics. Cambridge University Press, Cambridge, UK.

Bruinsma, R., A. Behrisch, and E. Sackmann. 2000. Adhesive switching of membranes: experiment and theory. *Phys. Rev. E.* 61:4253–4267.

Charitat, T., E. Bellet-Amalric, G. Fragneto, and F. Graner. 1999. Adsorbed and free lipid bilayers at the solid-liquid interface. *Eur. Phys. J. B.* 8:583–593.

Davis, D. M. 2002. Assembly of the immunological synapse for T cells and NK cells. *Trends Immunol.* 23:356–363.

Dietrich, C., L. A. Bagatolli, Z. N. Volvyk, N. L. Thompson, M. Levi, K. Jacobson, and E. Gratton. 2001. Lipid rafts reconstituted into model membranes. *Biophys. J.* 80:1417–1428.

Domb, C., and J. L. Lebwitz. editors. 1988. Phase Transitions and Critical Phenomena, Vol. 8. Academic Press, London, UK.

Evans, E., and E. Sackmann. 1988. Translational and rotational drag coefficients for a disk moving in a liquid membrane associated with a rigid substrate. *J. Fluid Mech.* 194:553–561.

Evans, E., and R. Skalak. 1980. Mechanics and Thermodynamics of Biomembranes. CRC Press, Boca Raton, FL.

Fragneto, G., T. Charitat, F. Graner, K. Mecke, L. Perino-Gallice, and E. Bellet-Amalric. 2001. A fluid floating bilayer. *Eur. Phys. Lett.* 53: 100–106.

Grakoui, A., S. K. Bromley, C. Sumen, M. M. Davis, A. S. Shaw, P. M. Allen, and M. L. Dustin. 1999. The immunological synapse: a molecular machine controlling T cell activation. *Science.* 285:221–227.

Groves, J. T., and S. G. Boxer. 2002. Micropattern formation in supported lipid membranes. *Acc. Chem. Res.* 35:149–157.

Groves, J. T., and D. L. Dustin. 2003. Supported planar bilayers in studies of immune cell adhesion and communication. *J. Immunol. Methods.* 278:19–32.

Hailman, E., W. R. Burack, A. S. Shaw, M. L. Dustin, and P. M. Allen. 2002. Immature $CD4^+CD^+$ thymocytes form a multifocal immunological synapse with sustained tyrosine phosphorylation. *Immunity.* 16: 839–848.

Hughes, B. D., B. A. Pailthorpe, and L. R. White. 1981. The translational and rotational drag on a cylinder moving in a membrane. *J. Fluid Mech.* 110:349–372.

Huster, D., P. Müller, K. Arnold, and A. Herrmann. 2001. Dynamics of membrane penetration of the fluorescent 7-nitrobenz-2-oxa-1,3-diazol-4-yl (NBD) group attached to an acyl chain of phosphatidylcholine. *Biophys. J.* 80:822–831.

Kahya, N., D. Scherfeld, K. Bacia, B. Poolman, and P. Schwille. 2003. Probing lipid mobility of raft-exhibiting model membranes by fluorescence correlation spectroscopy. *J. Biol. Chem.* 278:28109–28115.

Klingler, J. F., and H. M. McConnell. 1993a. Brownian motion and fluid mechanics of lipid monolayer domains. *J. Phys. Chem.* 97:6096–6100.

Klingler, J. F., and H. M. McConnell. 1993b. Field-gradient electrophoresis of lipid domains. *J. Phys. Chem.* 97:2962–2966.

Kloboucek, A., A. Behrisch, J. Faix, and E. Sackmann. 1999. Adhesion-induced receptor segregation and adhesion plaque formation: a model membrane study. *Biophys. J.* 77:2311–2328.

Krummel, M. F., and M. M. Davis. 2002. Dynamics of the immunological synapse: finding, establishing and solidifying a connection. *Curr. Op. Immunol.* 14:66–74.

Lakowicz, J. R. 1999. Principles of Fluorescence Spectroscopy. Kluwer Academic/Plenum Publishers, New York.

Lambacher, A., and P. Fromherz. 1996. Fluorescence interference-contrast microscopy on oxidized silicon using a monomolecular dye layer. *Appl. Phys. A.* 63:207–216.

Lambacher, A., and P. Fromherz. 2002. Luminescence of dye molecules on oxidized silicon and fluorescence interference contrast microscopy of biomembranes. *J. Opt. Soc. Am. B.* 19:1435–1453.

Lee, K.-H., A. D. Holdorf, M. Dustin, A. Chan, P. M. Allen, and A. S. Shaw. 2002a. T cell receptor signaling precedes immunological synapse formation. *Science.* 295:1539–1542.

Lee, S.-J. E., Y. Hori, and A. K. Chakraborty. 2003. Low T cell receptor expression and thermal fluctuations contribute to formation of dynamic multifocal synapses in thymocytes. *Proc. Natl. Acad. Sci. USA.* 100: 4383–4388.

Lee, S.-J. E., Y. Hori, J. T. Groves, M. L. Dustin, and A. K. Chakraborty. 2002b. Correlation of a dynamic model for immunological synapse formation with effector functions: two pathways to synapse formation. *Trends Immunol.* 23:492–499.

Lipowsky, R., and E. Sackmann. editors. 1995. Structure and Dynamics of Membranes. Elsevier Science Ltd., New York.

McCann, F. E., K. Suhling, L. M. Carlin, K. Eleme, S. B. Taner, K. Yanagi, B. Vanherberghen, P. M. W. French, and D. M. Davis. 2002. Imaging immune surveillance by T cells and NK cells. *Immunol. Rev.* 189:179–192.

McCann, F. E., B. Vanherberghen, K. Eleme, L. M. Carlin, R. J. Newsam, D. Goulding, and D. M. Davis. 2003. The size of the synaptic cleft and distinct distributions of filamentous actin, ezrin, CD43, and CD45 at activating and inhibitory human NK cell immune synapses. *J. Immunol.* 170:2862–2870.

Mecke, K. R., T. Charitat, and F. Graner. 2003. Fluctuating lipid bilayer in an arbitrary potential: theory and experimental determination of bending rigidity. *Langmuir.* 19:2080–2087.

Merkel, R., E. Sackmann, and E. Evans. 1989. Molecular friction and epitactic coupling between monolayers in supported bilayers. *J. Phys. Fr.* 50:1535–1555.

Monks, C. R. F., B. A. Freidberg, H. Kupfer, N. Sciaky, and A. Kupfer. 1998. Three-dimensional segregation of supramolecular activation clusters in T cells. *Nature.* 395:82–86.

Nardi, J., R. Bruinsma, and E. Sackmann. 1998. Adhesion-induced reorganization of charged fluid membranes. *Phys. Rev. E.* 58:6340–6354.

Papon, P., J. Leblond, and P. H. E. Meijer. 2002. The Physics of Phase Transitions. Springer, New York.

Parthasarathy, R., B. L. Jackson, T. J. Lowrey, A. P. Wong, and J. T. Groves. 2004. Nonequilibrium adhesion patterns at lipid bilayer junctions. *J. Phys. Chem. B.* In press.

Qi, S. Y., J. T. Groves, and A. K. Chakraborty. 2001. Synaptic pattern formation during cellular recognition. *Proc. Natl. Acad. Sci. USA.* 98: 6548–6553.

Sackmann, E. 1996. Supported membranes: Scientific and practical applications. *Science.* 271:43–48.

Sackmann, E., and R. Bruinsma. 2002. Cell adhesion as a wetting transition? *Chem. Phys. Chem.* 3:262–269.

Sackmann, E., and M. Tanaka. 2000. Supported membranes on soft polymer cushions: fabrication, characterization, and applications. *TIBS Tech.* 18:58–64.

Saffman, P. G. 1976. Brownian motion in thin sheets of viscous fluid. *J. Fluid Mech.* 73:593–602.

Saffman, P. G., and M. Delbrück. 1975. Brownian motion in biological membranes. *Proc. Natl. Acad. Sci. USA.* 72:3111–3113.

Stoll, S., J. Delon, T. M. Brotz, and R. N. Germain. 2002. Dynamic imaging of T cell-dendritic cell interactions in lymph nodes. *Science.* 296:1873–1876.

vanderMerwe, P. A. 2002. Formation and function of the immunological synapse. *Curr. Op. Immunol.* 14:293–298.

vanderMerwe, P. A, and S. J. Davis. 2002. The immunological synapse—a multitasking system. *Science.* 295:1479–1480.

Veatch, S. L., and S. L. Keller. 2002. Organization in lipid membranes containing cholesterol. *Phys. Rev. Lett.* 89:268101.

Wong, A. P., and J. T. Groves. 2001. Topographical imaging of an intermembrane junction by combined fluorescene interference and energy transfer microscopies. *J. Am. Chem. Soc.* 123:12414–12415.

Wong, A. P., and J. T. Groves. 2002. Molecular topography imaging by intermembrane fluorescence resonance energy transfer. *Proc. Natl. Acad. Sci. USA.* 99:14147.